Unveiling Extended Components of ‘Little Red Dots’ in Rest-Frame Optical

Yiyang Zhang[1], Xuheng Ding[1,*], Lilan Yang[2,*], Erini Lambrides[3], Hollis Akins[4], Andrew J. Battisti[5,6], Caitlin M. Casey[7,8], Chang-hao Chen[9,10], Isa Cox[2], Andreas Faisst[11], Maximilien Franco[12], Aryana Haghjoo[13], Luis C. Ho[9,10], Kohei Inayoshi[9], Shuowen Jin[8,14], Mitchell Karmen[15], Anton M. Koekemoer[16], Jeyhan S. Kartaltepe[2], Kai Liao[1], Ghassem Gozaliasl[17,18], Masafusa Onoue[19,20], Vasily Kokorev[4], Namrata Roy[21,22], R. Michael Rich[23], John D. Silverman[24], Takumi S. Tanaka[24,25], Bei You[1], Hassen M. Yesuf[26], and Jorge A. Zavala[27]

[1]School of Physics and Technology, Wuhan University, Wuhan 430072, China
[2]Laboratory for Multiwavelength Astrophysics, School of Physics and Astronomy, Rochester Institute of Technology, 84 Lomb Memorial Drive, Rochester, NY 14623, USA
[3]NASA-Goddard Space Flight Center, Code 662, Greenbelt, MD, 20771, USA
[4]Department of Astronomy, The University of Texas at Austin, Austin, TX 78712, USA
[5]International Centre for Radio Astronomy Research, University of Western Australia, 35 Stirling Hwy, Crawley, WA 6009, Australia
[6]Research School of Astronomy and Astrophysics, Australian National University, Cotter Road, Weston Creek, ACT 2611, Australia
[7]Department of Physics, University of California, Santa Barbara, Santa Barbara, CA 93106, USA
[8]Cosmic Dawn Center (DAWN), Denmark
[9]Kavli Institute for Astronomy and Astrophysics, Peking University, Beijing 100871, China
[10]Department of Astronomy, School of Physics, Peking University, Beijing 100871, China
[11]Caltech/IPAC, MS 314-6, 1200 E. California Blvd. Pasadena, CA 91125, USA
[12]Université Paris-Saclay, Université Paris Cité, CEA, CNRS, AIM, 91191 Gif-sur-Yvette, France
[13]Department of Physics and Astronomy, University of California Riverside, Riverside, CA 92521, USA
[14]DTU Space, Technical University of Denmark, Elektrovej 327, 2800 Kgs. Lyngby, Denmark
[15]Department of Physics and Astronomy, Johns Hopkins University, Baltimore, MD 21218, USA
[16]Space Telescope Science Institute, 3700 San Martin Drive, Baltimore, MD 21218, USA
[17]Department of Computer Science, Aalto University, P.O. Box 15400, FI-00076 Espoo, Finland
[18]Department of Physics, University of Helsinki, P.O. Box 64, FI-00014 Helsinki, Finland
[19]Waseda Institute for Advanced Study (WIAS), Waseda University, 1-21-1, Nishi-Waseda, Shinjuku, Tokyo 169-0051, Japan
[20]Kavli Institute for the Physics and Mathematics of the Universe (Kavli IPMU, WPI), UTIAS, Tokyo Institutes for Advanced Study, University of Tokyo, Chiba, 277-8583, Japan
[21]Center for Astrophysical Sciences, Department of Physics and Astronomy, Johns Hopkins University, Baltimore, MD 21218, USA
[22]School of Earth and Space Exploration, Arizona State University, Tempe, AZ 85287, USA
[23]Department of Physics and Astronomy, UCLA, PAB 430 Portola Plaza, Los Angeles, CA 90095-1547, USA
[24]Kavli Institute for the Physics and Mathematics of the Universe (WPI), The University of Tokyo, Kashiwa, Chiba 277-8583, Japan
[25]Department of Astronomy, Graduate School of Science, The University of Tokyo, 7-3-1 Hongo, Bunkyo-ku, Tokyo, 113-0033, Japan
[26]Key Laboratory for Research in Galaxies and Cosmology, Shanghai Astronomical Observatory, Chinese Academy of Sciences, 80 Nandan Road, Shanghai 200030, China
[27]University of Massachusetts Amherst, 710 North Pleasant Street, Amherst, MA 01003-9305, USA
[*]e-mail: dingxh@whu.edu.cn, lxysps@rit.edu

Recent JWST observations have revealed a population of red, compact, high-redshift objects called “Little Red Dots” (LRD), whose host components have remained largely unconstrained, possibly due

to their extreme compactness. Current morphological studies have been limited by small samples, as well as by insufficient imaging depth, which may not allow reliable separation between point-like and extended components, leaving the existence and properties of extended components in LRD largely unconstrained. Here, we perform the image stacking analysis of 217 LRDs in four NIRCam bands, representing the largest and homogeneous sample observed from COSMOS-Web survey to date. Our results reveal an unambiguous detection of faint extended emission in the F444W band, with a typical size of $\sim$200 parsecs and magnitude of $\sim$27.7 AB at z$\sim$6.5. We perform four-band photometric SED fitting based on galaxy templates and derive a stellar mass of $10^{8.91^{+0.10}_{-0.11}}$ M$\odot$. Given this stellar mass, the host galaxy is compact, i.e., $\sim$2.5 times smaller than star-forming populations at similar mass, and the typical black hole mass of LRDs is elevated by $\sim$1.5 dex above the local M_{BH}-M_* relation. This work provides direct observational evidence for the existence of LRD host galaxies and offers crucial insights into the growth of the host galaxy and the co-evolution of galaxies and their black holes within the first billion years after the Big Bang.

The discovery of extremely compact, red sources with a characteristic V-shape SED at high redshift, commonly referred to as Little Red Dots (LRD), has opened a new window into the assembly of the earliest black holes and their environments[1,2,3]. Constraining the nature of their extended host galaxies is essential for understanding the co-evolution of galaxies and black holes in the early universe. Current theoretical interpretations of LRD remain diverse, and establishing the presence and properties of their host galaxies is crucial for resolving their nature. Yet it remains uncertain whether all LRDs possess such host. Initial evidence has been reported for individual cases[4,5,6,7,8], but a direct detection of the extended host is needed to establish their overall presence and properties. In particular, detection in the rest-frame optical regime is regarded as compelling evidence for stellar emission.

We started with a parent sample of 434 LRDs, spanning a redshift range of $z \sim 5$–9, originally identified in the COSMOS-Web field[9]. The COSMOS-Web program provides deep imaging with JWST/NIRCam and MIRI over a uniquely large survey area, enabling the construction of a statistical sample of LRD. In this study, we focus on NIRCam data in four wide-band filters—F115W (1.15 μm), F150W (1.50 μm), F277W (2.78 μm), and F444W (4.44 μm), because NIRCam offers significantly wider coverage, whereas many LRD lack corresponding MIRI imaging. These NIRCam filters allow us to probe the rest-frame ultraviolet (UV) and optical emission at $z > 5$. The 5σ depth in $0.''15$ radius aperture ranges from 26.7 to 27.5 mag in F115W and 27.5 to 28.2 mag in F444W, depending on the number of integrations[10].

To refine our sample for analysis, we apply three selection criteria to the parent sample: a color cut (F115W $-$ F150W < 0.8) to select sources with prominent UV-excess features[3,11], a magnitude limit ($\mathrm{mag_{total}} < 30$) to ensure sufficient signal-to-noise ratio (SNR), and a requirement of good imaging fit quality (reduced $\chi^2 < 2$; see Methods).Our final sample comprises 217 LRDs with robust photometry across all four NIRCam bands, meeting stringent quality criteria. Although this is a carefully selected subset, it remains the largest dataset of LRD employed for morphological analysis to date. Additionally, to examine the potential bias due to variability, we inspected a subsample of 18 LRDs with multi-epoch imaging. We find there is no significant variation with time across all NIRCam bands with typical magnitude differences below 0.2 mag, consistent with previous studies[12,13] (see Methods).

In our image analysis, we adopt the NIRCam mosaics with pixel scale of $0.''03$, and the details of the imaging data reduction are summarized in Franco et al.(2025)[14]. The fitting is conducted on cutouts of 31×31 pixels for the short-wavelength bands (F115W, F150W) and 61×61 pixels for the long-wavelength bands (F277W, F444W), respectively, to account for their different spatial resolutions. During the fitting process, we use PSF models generated with PSFEx[15], which models spatial PSF variations across the field as a polynomial function of pixel coordinates by fitting multiple stars simultaneously. We adopt `galight` (v0.2.1) software package[16] for two-dimensional image analysis.

The observed morphologies of LRDs are typically compact and dominated by the point source[6,17]. It is challenging to recover the extended emission of LRDs through individual fitting due to their faintness[2]. To illustrate how closely the LRD profiles resemble a pure point source, we first modeled each source using a single point source (PS-only) across all four NIRCam bands. If an extended component is present, we expect to see residual images showing central over-subtraction and excess emission in the outskirts, i.e., signatures of extended light not accounted for by the point source model. However, there is no evident emission in the residual map for an individual LRD as shown in the top-left panel of Figure 1, probably resulting from low SNR.

We then stacked the residual images, obtained by subtracting the point source model and any nearby sources, for all selected LRDs, thereby enhancing the signal-to-noise ratio and making faint extended emission more detectable, as shown in Figure 1. Remarkably, we observed a clear ring-like excess flux in the outskirts, indicating light components not fully captured by a single point source. To further verify the detection of this flux excess, we constructed its corresponding SNR map. Specifically, we constructed an error map by combining the background noise with the standard deviation of PSFs sampled from 20 different COSMOS-Web regions. The resulting SNR map is presented in Figure 1 (right panel). The ring feature reaches a total SNR of 72.19, establishing the statistical significance of the extended emission and providing compelling evidence for the existence of the extended emission. Additionally, to rule out the possibility that the excess is caused by fitting uncertainties such as PSF mismatch, we performed a control test by stacking the residuals using 263 stars after the same procedure to verify that the 'ring' structures seen in LRD are not artifacts of PSF modeling (see Extended Data Figure 4).

Having confirmed the presence of extended components, we carry out two-dimensional decomposition for all LRDs using the PS+Sérsic profile across all four NIRCam bands to characterize the properties of their extended emission[18]. To prevent unphysical solutions for the Sérsic parameters[19], we impose boundaries on key parameters as follows: $R_{\rm eff} \in [0''.03, 0''.1]$ (100–600 pc at z $\sim$ 6.45), $n \in [1,4]$, and eccentricity $e_1, e_2 \in [-0.3, 0.3]$. The Sérsic centroid was allowed to vary within 2 pixels to account for small positional shifts. For nearby companions, we introduced additional Sérsic components to subtract contaminating flux, without imposing constraints on their fitting parameters. Based on the results of the PS+Sérsic fitting described above, we derived the extended emission to total flux ratio distributions for all LRDs across the four NIRCam bands (see Extended Data Figure 2, left panel). The result shows that the median values of the flux ratio decreases systematically from $\sim$60% in F115W to $\sim$12% in F444W, indicating the extended emission contributes significantly in the blue bands ($< 2\,\mu$m) while the red bands ($> 2\,\mu$m) are dominated by the AGN emission[20].

To robustly characterize the properties of the extended emission, we study the stacked extended emission of 217 LRDs across four bands, i.e., data minus PS model and any nearby sources, as shown in Figure 2 (top panels). During this process, the residual images are aligned based on the centroid of the point source prior to stacking, ensuring accurate registration of the extended emission (see Methods).We then fit the stacked image with a single Sérsic model, treating the resulting parameters as representative of the average extended emission properties (see Figure 2, middle panels). The best-fit Sérsic parameters (magnitude, effective radius $R_{\rm eff}$, Sérsic index n), and extended emission to total flux ratio, are summarized in Table 1. The average magnitude of the extended component is close to 29 mag, which is well below the individual detection threshold of the COSMOS-Web 5σ detection limits (27.4–28.2 AB mag). This, again, demonstrates the importance of the stacking approach for enhancing the SNR to achieve a statistically significant measurement of the extended component. Simulation tests further confirm that the stacking and fitting procedure can reliably recover the input extended emission parameters to within 0.1 mag in magnitude and 0.1 dex in size (see Extended Data Figure 5), ruling out PSF mismatches or stacking artifacts as the source of the observed extended emission.

The size of the stacked image is $\sim$210 pc in rest-frame optical (F444W) and increases toward shorter wavelength, i.e., $\sim$392 pc in rest-frame UV (F115W). This trend of wavelength dependence indicates that the UV emission, which traces recent star-forming regions, is more extended than the underlying stellar distribution probed by the optical light. Such an extended UV component might suggest ongoing star formation in the outskirts of the host galaxy, consistent with that reported by Rinaldi et al.(2025)[4] and Chen et al. (2025)[7].

The extended emission to total flux ratios of the stacked image are approximately 10-20% in longer wavelengths, further confirming the strong AGN dominance. In shorter wavelengths (rest-frame UV), the extended emission to total flux ratios reach 40%. The significant contribution from the extended emission is consistent with the BH–star model hypothesis[22], which suggests that the rest-frame UV part of the V-shaped SED mainly originates from the galaxy, with the overall V-shaped SED arising from the combination of galaxy and BH–star contributions.

We utilize the inferred four-band photometry of the stacked source and performed spectral energy distribution (SED) fitting to clarify its physical origin. We first interpret the extended emission as originating from stars and adopt a single combined stellar population model at an average redshift of $z = 6.45$. We use `bagpipes`[23] to perform SED fitting. The stellar metallicity is allowed to vary between 0 and $2.5Z_{\odot}$, the stellar age is constrained to $[0.01, 0.85]$ Gyr (capped by the age of the Universe at the source redshift), and the dust attenuation is modeled with a Calzetti law, with A_V free to vary in the range $[0, 5]$ mag. Our result indicates that the stacked host of LRDs is consistent with a star-forming galaxy with a stellar mass M_* of $10^{8.91^{+0.10}_{-0.11}} M_{\odot}$ and the star formation rate of SFR $\sim 1.81^{+0.68}_{-0.41} M_{\odot}\,\mathrm{yr}^{-1}$ (see Figure 3). The inferred properties of the host match with the expected mass range $10^{8.5}$ to $10^{10} M_{\odot}$ of star formation–dominated LRDs as reported in Akins et al.(2024)[9], and also agree with the $\sim 10^9 M_{\odot}$ stellar mass of an unusually bright dust-reddened AGN host galaxy reported by Wang et al.(2024)[24]. We have also verified the robustness of our results by cross-checking them with other SED fitting codes, such as `gsf`[25], yielding consistent outcomes.

To investigate the potential cosmic evolution of host properties, we have also performed SED fittings of stacked images in two redshift bins $5 < z < 6.4$ (1.19 – 0.87 Gyr) and $7 < z < 9$ (0.87 – 0.55 Gyr), respectively. We find the median stellar masses are $10^{8.77^{+0.13}_{-0.15}} M_{\odot}$ and $10^{9.16^{+0.10}_{-0.11}} M_{\odot}$, respectively, which may suggest a slight evolution, although the specific star formation rates (sSFR) remain consistent between the two bins. However, the excess in the bluer band is more pronounced at lower redshift, possibly indicating a younger host galaxy or the emergence of AGN-driven ionized bubbles[26].

Although some theoretical models predicted that LRDs should exhibit significant dust emission, our host SED fitting does not require such a component; this is consistent with our low A_V inference and with multiple recent studies reporting negligible dust emission in LRDs. Observations from ALMA and JWST/MIRI have systematically explored the mid- and far-infrared properties of LRDs, consistently revealing limited dust content in these sources[27,28,29]. Furthermore, empirical relations between stellar mass and dust mass suggest that, given their relatively low stellar masses, LRDs host are expected to have dust masses below $10^6\ M_{\odot}$[30,31]. Such low dust masses likely result in dust emission levels below current ALMA detection limits, providing a natural explanation for the lack of significant dust signatures in these systems.

We also tested an SED fit with a nebular gas model, but it could not reproduce the extended emission in F444W and predicts strong emission lines that lack observational support (see Extended Data Figure 7). Therefore, we consider the solution by the stellar model to be the more plausible interpretation.

Based on measured size R_{eff}, the host galaxy is compact in rest-frame optical with 210$\pm$26 pc at an average redshift of $z = 6.45$. Combining the inferred stellar mass, we compare its result with the size–mass distribution at $6 < z < 7$ of star-forming galaxies (SFGs) obtained in the same COSMOS-Web field[32]. As shown in Figure 4, LRD host occupies the lower-mass end of the distribution, with sizes among the smallest ones observed at these stellar masses. In the mass range of $\log(M_*/M_\odot) = 8.6$–9.0, the median size of SFGs is 518 pc, approximately 2.5 times larger than that of LRD host. The compact nature suggests that the host galaxies have undergone concentrated star formation and have assembled a substantial portion of their stellar mass in their central region. The build-up of the dense gas in the core naturally fuels the central supermassive black hole, triggering the ignition of AGN. However, the measured rest-frame UV size of $\sim$400 pc is extended and much larger than that in rest-optical. According to SED analysis, the extended UV emission could be either dominated by a young stellar population with low dust attenuation or by strong nebular emission. In the former case, the outskirts of the host are likely undergoing recent star formation, leading to a larger UV size than optical, which could also provide evidence for the early stage of inside-out galaxy growth. On the other hand, the latter case suggests an overestimation of stellar mass size, although this scenario is less favored.

Several studies have inferred that LRDs harbor black holes with masses on the order of 10^7 to $10^8\ M_\odot$[24,33,34]. Compared to the stellar masses derived from our SED fitting, these black hole masses lie significantly above the expectations from the local $M_{\rm BH}$–M_* relation[35,36], which shows that black hole masses that are typically 2 to 3 orders of magnitude lower than their host stellar masses, as illustrated in Figure 4. This discrepancy suggests that LRD may harbor heavy black hole seeds, formed through mechanisms distinct from those producing lighter seeds[37,38]. The overmassive black holes relative to their compact, low-mass host imply rapid black hole growth that outpaces stellar mass assembly. This scenario aligns with theoretical models in which massive black hole seeds form via direct collapse, bypassing the intermediate stellar phase and enabling the early emergence of supermassive black holes within the first billion years after the Big Bang[39,40]. However, the black hole masses adopted here are based on literature estimates, typically assuming dust-obscured AGN with $A_V \sim 3$, and are highly model-dependent. If future observations favor a dust-free scenario[41,42], the inferred $M_{\rm BH}/M_*$ ratios would be reduced, could be substantially reduced, potentially bringing LRD in line with the local relation.

Figures

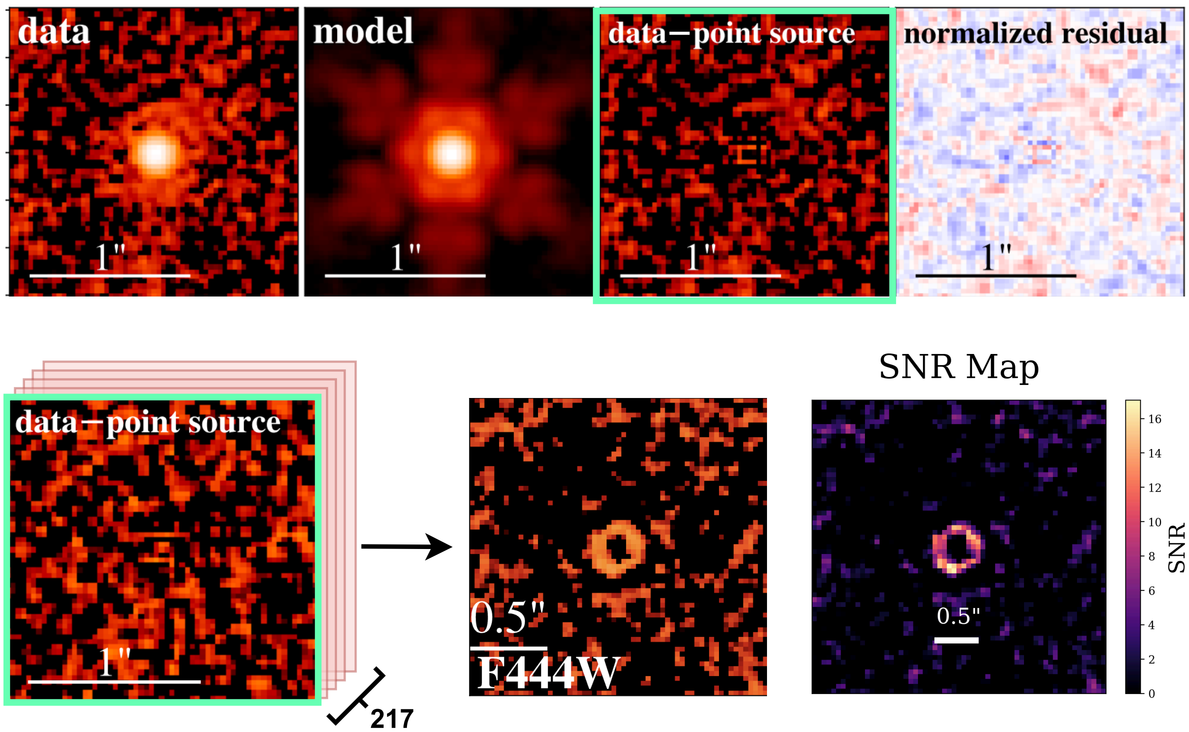

Figure 1. Imaging stacking analysis reveals the underlying extended emission that is not clearly detectable in individual PS-only decompositions. *Top left:* An example of 2D decomposition for an individual LRD using a PS-only model. From left to right: original LRD image (data), model image generated from the PSF (model), residual image after subtracting the point source component (data−PS), and the normalized residual. *Bottom left:* Illustration of the stacking procedure. Residuals (data−PS) from 217 LRDs are aligned and averaged to produce a stacked image that enhances the visibility of low-surface-brightness extended emission in the outskirts. *Right:* The SNR map of the residual feature. The standard deviation image (error map) is computed by measuring pixel-by-pixel dispersion across different PSFs at the same location and corresponding background noise. The stacked data−PS image is used as the signal in this calculation.

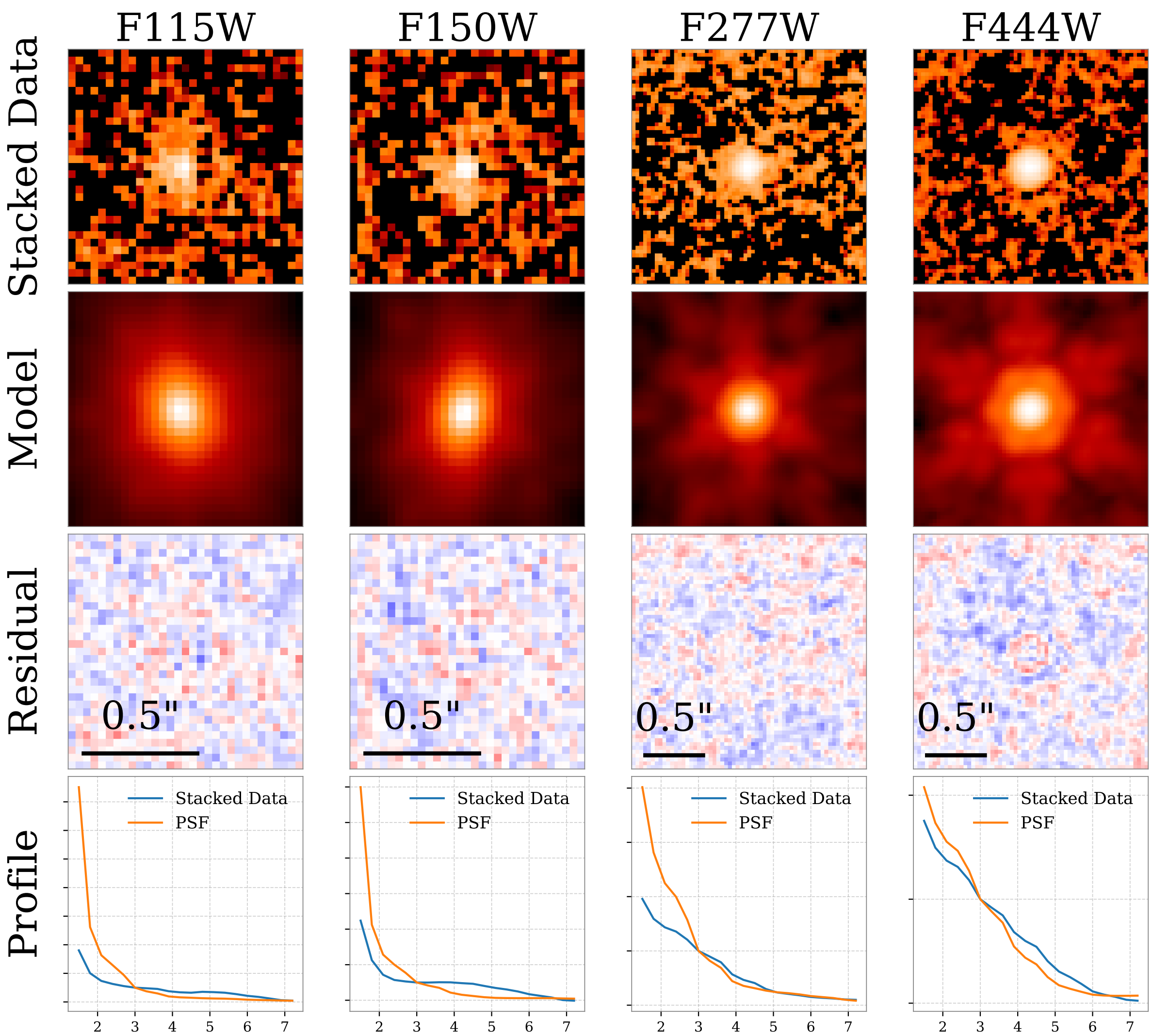

Figure 2. Imaging modeling of stacked image across four NIRCam bands. Stacked data-PS residual image based on PS + Sérsic fitting, representing the average extended emission of LRD. Each panel corresponds to one of the four NIRCam filters (F115W, F150W, F277W, and F444W), illustrating the wavelength-dependent morphology of the mean extended component. *Top:* Stacked image across the four NIRCam bands (averaged). A scale bar of $0.5''$ corresponds to 2.8 kpc at $z \sim 6.45$. *Middle:* Best-fit models using a single Sérsic model. *Third row:* Corresponding normalized residuals. *Bottom:* Azimuthally averaged light profiles of the stacked data (blue) compared to the PSF (orange).

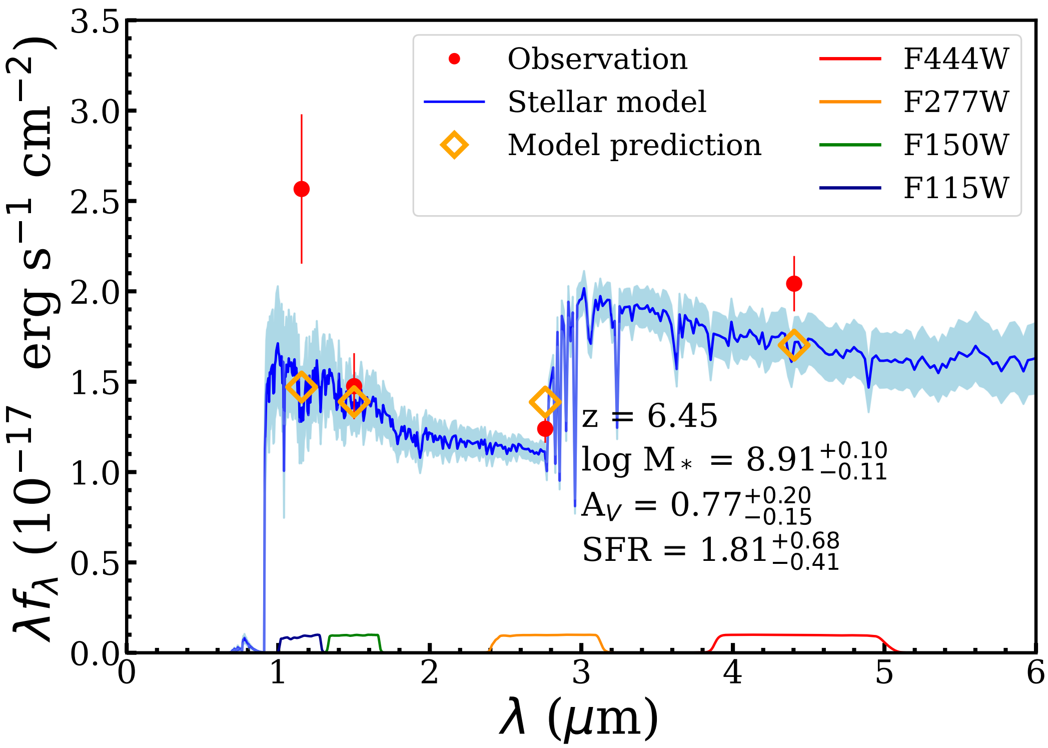

Figure 3. **SED fitting of the extended emission using four-band photometry based on galaxy templates via `Bagpipes`.** Red data points with error bars show the inferred host fluxes. The blue region indicates the 1σ uncertainty range of the SED templates derived from Markov-Chain Monte-Carlo (MCMC) sampling, represents the stellar template, with orange diamonds marking the predicted fluxes from this template.

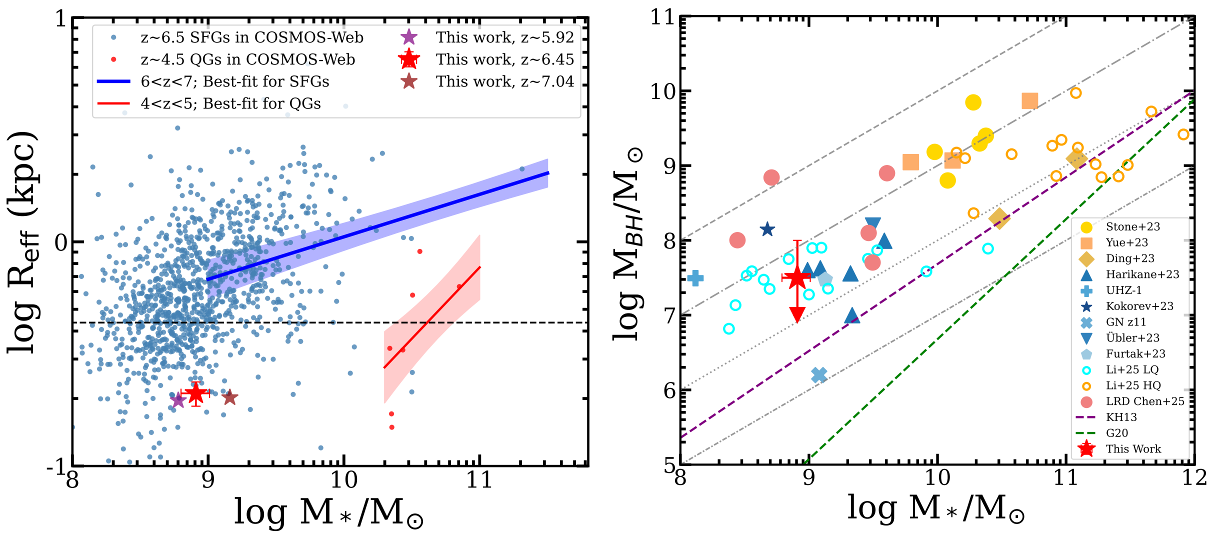

Figure 4. Locations of the LRD host galaxy on the size–mass and M_{BH}–M_* relations. *Left:* Size–mass relation of galaxies and LRD host in the COSMOS-Web field. Blue and red points represent star-forming galaxies (SFGs) at $z \sim 6.5$ and quiescent galaxies (QGs) at $z \sim 4.5$, respectively[32]. The blue and red lines show the best-fit size–mass relations for SFGs with $M_* > 10^9\,M_\odot$ and QGs. LRD host exhibit systematically smaller sizes compared to other star-forming galaxies of similar stellar mass, suggesting that their structural growth may still be in an early stage. Purple stars indicate measurements using the redshift bin $z = 5$–6.4 (mean $z = 5.92$), while dark red stars indicate measurements using the redshift bin $z = 6.4$–9 (mean $z = 7.04$). *Right:* M_{BH}–M_* relation, shown in comparison with $z > 5$ quasars in the literature. The red marker (i.e., this work) is based on the typical M_{BH} range of 10^7–10^8 $M_\odot$ for LRD[24,33,34], indicating a potential deviation from the local relation. Literature quasars are shown as blue and yellow markers[33,43,44,45,46,47,48,49], where LQ and HQ denote low- and high-luminosity quasars, respectively. Light-coral points indicate individually detected host galaxies of LRDs[7]. The purple and green dashed lines correspond to the local relations from Kormendy and Ho et al.(2013)[35] and Greene et al.(2020)[36], respectively.

Tables

Filter	Magnitude	$R_{\rm eff}$ (arcsec)	Size (pc)	Sérsic index (n)	Flux ratio
F115W	28.913 ± 0.173	0.070 ± 0.011	392.0 ± 59.0	1.659 ± 0.346	39.6%
F150W	29.229 ± 0.131	0.062 ± 0.005	344.9 ± 30.7	2.002 ± 0.303	33.9%
F277W	28.756 ± 0.064	0.043 ± 0.004	240.8 ± 23.5	1.000 ± 0.196	23.2%
F444W	27.707 ± 0.079	0.038 ± 0.005	210.6 ± 26.2	1.000 ± 0.0001	11.8%

Table 1. Properties of LRD stacked-image across different filters. All uncertainties are derived from simulations (see Extended Data Figure 5). Sizes (pc) are converted assuming a redshift of $z = 6.45$. Flux ratio refers to the extended emission to total flux ratio, values are the averages from the stacked image, as indicated in Extended Data Figure 2.

Methods

Target selection and data imaging. Our dataset is from COSMOS-Web survey, the largest imaging survey 0.54 deg^2 in NIRCam in the JWST Cycle 1 treasury program. The COSMOS-Web survey[10,50] (GO:1727, PI: J. Kartaltepe and C.Casey) covers a part of the COSMOS field[51] with NIRCam[52] in four filters (i.e., F115W, F150W, F277W, and F444W) with approximate 5σ depths ranging from 27.4 to 28.2 AB mag[50]. Our parent LRD samples consist of 434 sources identified by Akins et al.(2024)[9]. Those sources were selected based on a compactness criterion, $C_{444} = f_{444}(d = 0.2'')/f_{444}(d = 0.5'')$, and a red color criterion of $F277W - F444W > 1.5$, designed to collect isolate compact sources with significant red colors.

In this work, to capture prominent UV-excess features and to ensure robust photometric measurement, we further refined the sample by applying three additional selection criteria: (1) a blue color cut of $F115W - F150W < 0.8$; (2) a magnitude cut $\mathrm{mag_{total}} < 30$ to guarantee sufficient signal-to-noise ratio for reliable analysis; and (3) a goodness-of-fit threshold with reduced $\chi^2 < 2$ based on PS+Sérsic fitting (see next two subsections for details). These criteria reduce our final sample to 217 LRDs, which have high-quality, homogeneous photometric measurements across four NIRCam bands, representing the largest such dataset to date for detailed morphological analyses. We also performed a test without applying the first criteria (i.e., color selection), resulting in a sample of 357 LRDs. The derived magnitudes and sizes remain consistent (< 0.2 mag and < 0.1 dex, respectively) with those from our main analysis, except for F115W in which the inferred extended component in the short-wavelength bands appears fainter due to the absence of the V-shape selection. Nevertheless, the inferred stellar mass remains robust and consistent across samples.

The data presented in this work is taken with Module A and Module B of the NIRCam instrument, which has a field of view of 2.2×2.2 square arcminutes for each module. Images in the four bands (F115W, F150W, F277W and F444W) were drizzled to a pixel scale of $0.''03$[14,53,54,55,56].

2D image fitting preparation. We carried out 2D image analysis on all parent sample including 434 LRDs from the COSMOS-Web field using the open-source Python package `galight` software, which utilizes the image modeling capabilities of `lenstronomy`[57]. To account for different spatial resolutions across filters at different wavelengths, we adopted different cutout sizes. Specifically, the F444W and F277W images were cropped to 61×61 pixels, while the F150W and F115W images were cropped to 31×31 pixels. The global background light subtraction is first performed using the `Background2D` function of `Photutils`[58]. Since our method involves combining and stacking data from over 200 images, even a negligible background light present in individual sources can be amplified and become significant in the final stacked image. To address this, we applied an additional flat background correction to each LRD image to ensure that the background light in the empty region remained statistically neutral after model fitting. This step ensures an unbiased fitting for both the total flux and the R_{eff}, defined here as the semi-major-axis half-light radius of the Sérsic component.[59].

Since the COSMOS-Web field is divided into multiple subregions (A1–A10 and B1–B10), we applied region-specific PSF models for each target to match the local optical response. As JWST mirrors are rephased every few weeks, minor PSF variations across epochs may introduce small systematic uncertainties, though these are expected to average out in the stacking process. We construct PSF models using `PSFEx`[15], which fits multiple point sources simultaneously and allows modeling of spatial PSF variations across the field of view as a polynomial function of pixel coordinates. To capture potential variations across the COSMOS-Web area, we generate separate PSF models for 20 sub-regions, which are adopted in the subsequent morphological fitting. These PSF models have also been utilized in other COSMOS-Web studies (Tanaka et al.[21,60], Yang et al.[32], Zhuang et al.[61]).

Fitting strategies. Two different fitting models were employed to fit the data: (1) a PS-only model, where the entire flux distribution is represented by a single PSF component, and (2) a composite model consisting of a PSF component and a single Sérsic profile convolved with the PSF. In this second model, the Sérsic model is used to capture the extended component of LRD.

The Sérsic component includes seven free parameters: amplitude, Sérsic index n, effective radius $R_{\rm eff}$, central coordinates (x_c, y_c), and eccentricity parameters (e_1, e_2). To avoid unphysical parameter inference, we applied constraints to the Sérsic profile parameters. Regardless of the fitting method (PS-only or PS+Sérsic), the initial source coordinates (x_c, y_c) were adopted from Akins' catalog[9]. For the PS+Sérsic fits, we limit the Sérsic centroid deviation to within 2 pixels of the PSF center to avoid positional shifts due to low SNR and background contamination. The effective radius $R_{\rm eff} \in [0.''03, 0.''1]$ (i.e., from one pixel to up to 600 pc) to prevent overestimation due to noise. Given the intrinsic compactness of LRD, unconstrained fitting often resulted in unrealistically high n values ($n > 8$). We thus set the Sérsic index $(n) \in [1, 4]$, consistent with typical morphological expectations: $n = 1$ represents disk-like structures, while $n = 4$ corresponds to classical bulges. The eccentricity parameters e_1 and e_2 were limited to the range -0.3 to 0.3 to maintain physically plausible ellipticities. For the LRD with any nearby object in the cutout, we simultaneously fit with another Sérsic profile with no constraints, allowing us to remove its light during the stacking.

Results of individual source fitting. We fit each source via two fitting strategies introduced above. For illustration, we present in Extended Data Figure 3 the fitting results for an example source in the F444W filter. The figure compares the results obtained using the PS-only model (top panel) and the PS+Sérsic model (bottom panel). For the same target, the PS+Sérsic model reveals extended emission, while the PS-only model also yields comparably good residuals. We compare the Bayesian Information Criterion (BIC) of those two fittings, and show no significant difference in goodness-of-fit between the two models; this result holds across the entire parent LRD sample. This similarity is likely due to the faintness of the extended emission and the limited SNR in individual sources, which constrain the ability of the BIC to distinguish the models. In the following subsection, we show that fitting individual LRD using a PS-only model provides compelling evidence for extended components in higher SNR data produced by stacking.

We now examine the significance of the extended emission revealed by PS+Sérsic modeling and its distribution across four NIRCam filters. Specifically, for sources with $\chi^2 < 2$ based on PS+Sérsic fitting, we derived the extended emission to total flux ratio based on the decomposition model, defined as the fraction of flux between the Sérsic component and total, i.e., PS+Sérsic. The distribution of extended emission to total flux ratio across four bands of the final selected 217 LRDs is shown in Extended Data Figure 2 (left panel). The distribution skews toward larger values (70%–80%) at F115W and F150W, however skews to smaller values at F277W and F444W. For example, the distribution at F444W peaks at $\sim 10\%$. The larger fraction of LRD has a higher extended emission to total flux ratio at shorter-wavelength filters, whereas this ratio decreases substantially towards longer-wavelength filters. To investigate the redshift dependence of the extended emission to total flux ratio, we divided the LRD sample into redshift bins of width $\Delta z = 0.5$, spanning the range $5 < z < 9$. For each of the four *JWST*/NIRCam bands (F115W, F150W, F277W, and F444W), we computed the mean value within each redshift bin and presented in Extended Data Figure 2 (right panel).

Unveils faint extended emission via image stacking. We employed a stacking method to enhance the SNR in the residual maps of LRD$-$PS image. Statistically, the signal increases linearly with the number of stacked images N, and the noise grows only as $\sqrt{N}$, leading to an overall enhancement $\propto \sqrt{N}$, which is $\sqrt{217}$ according to our sample size. We collected the residual maps obtained by subtracting the best-fit point source from each LRD and stacked these images, aligning them based on the LRD center positions.

To minimize contamination, we also subtract flux from neighboring objects within the field of view. This ensures that the final stacked image predominantly contains only background noise and any genuine extended emission. We perform a simple (unweighted) average stack of the residual images of 217 LRDs, according to our target selection. The resulting stacked image is normalized by the number of adopted sources, representing a high-SNR image highlighting any extended structures after removing the PSF model. Before stacking, each residual image is shifted based on the centroid position of the point source. The shifting is performed through direct pixel translation without interpolation, such that the image is moved in integer pixels along both axes and the regions moved out of the frame are filled with zeros. The COSMOS-Web survey was conducted in three epochs between January 2023 and January 2024. For LRD objects observed multiple times in overlapping regions, we perform the fitting for all the data, however, for the stacking, we only use the one in the earliest observation. Since we adopt two fitting models, we show the stacked residual image for both models.

We first present the image stacking results for the PS-only model. As shown in Figure 1, we demonstrate the stacking method and SNR map of the stacked residual image at the F444W band. Our stacked image reveals significant over-subtraction in the central region, characterized by negative flux, indicating that the point source profile inferred by the PS-only model overestimates the central flux. Meanwhile, the residual light in the outskirts forms a positive flux 'ring' feature with a typical radius of $\sim$0.2 arcsec, suggesting the presence of extended emission that cannot be accounted for by a single point source. This outcome is expected when the fitted data contains unresolved extended components that the PS-only model fails to capture. To verify that the ring feature is not an artifact caused by PSF mismatch to the data, we calculated the flux ratio of the ring feature and compared it to the standard deviation of the PSFs derived from all PSFs in the COSMOS-Web field. We find that the flux level of the ring feature exceeds the PSF uncertainty at the corresponding region, with a SNR of approximately 10. This result provides strong evidence for the presence of extended emission in the stacked LRD sample, which cannot be explained by PSF uncertainty.

Given the confirmed presence of extended components, the PS+Sérsic model should provide a more accurate fit to our LRDs. As shown in Figure 2, we now perform the residual stacks derived from data$-$PS component obtained from PS+Sérsic modeling, across all four bands (F115W, F150W, F277W, and F444W) (see Figure 2, top panel). This provides a clearer view of the extended emission structure, enabling more detailed subsequent analyses. We estimate the SNR of the stacked image in each band. The measured SNRs are 5.2, 8.3, 16.2, 34.4 in F115W, F150W, F277W, and F444W, respectively, indicating that the extended emission detections are statistically significant, particularly in the longer-wavelength bands, where the extended emission is more pronounced.

We also estimated the stacked extended emission to total flux ratio. During this process, we calculated the flux of the stacked extended component divided by that of the stacked point-source component. As shown in Extended Data Figure 2, due to the lower SNR of individual LRD in the shorter-wavelength bands, many sources were misidentified as having high extended emission to total flux ratios during individual fitting, resulting in a significant discrepancy between the stacked ratio and the median of the individual measurements. Based on the stacked extended emission to total flux ratio, the point-source component clearly dominates in the longer-wavelength bands, contributing up to 90% of the total flux. Even in the shorter-wavelength bands, the flux is not entirely from the extended emission, suggesting that additional mechanisms beyond extended emission may contribute to the rising side of the LRD's characteristic V-shape. More detailed photometric measurements of the stacked image are presented in the next subsection.

We acknowledge that the LRD positions are not always precisely centered on a pixel, which may introduce some dispersion in the final stacked image size. we have examined the distances between the Sérsic component (representing the extended emission) and the point source in individual fits, and found that most offsets are around 1 pixel and remain within 2 pixels, indicating that the miscentering is generally small. In our analysis, we adopted the point-source coordinates as the centering reference and directly aligned the LRDs without interpolation. This strategy mitigated potential biases in size measurements that could otherwise arise from shifting the extended emission component.

Validating the PSF model accuracy using star images. To assess whether the ring-like signal observed in the PS-only stacked residual image of LRD could be artifacts introduced by the fitting procedure or PSF modeling, we conducted a control test using a star from the same COSMOS-Web field. We selected 263 isolated, unsaturated stars with F444W magnitudes fainter than 24 mag to ensure a fair comparison with the LRDs in terms of S/N and flux level. Each star was modeled using the same PS-only fitting procedure and the corresponding PSF from PSFEx as applied to the LRD sample. The fitted residual images were stacked following the same stacking procedure described in main text.

The resulting stacked residual image of stars exhibits no significant extended structures or 'ring'-like patterns, appearing compact and symmetric as in Extended Data Figure 4. This contrasts with the LRD residual stack and confirms that the residual features in LRD are not due to fitting artifacts or imperfections in the PSF model, but instead reflect real extended emission beyond the point source.

Photometry and morphology of the stacked extended emission. We begin by measuring the apparent sizes of the extended emission and comparing them to the corresponding PSFs. The full width at half maximum (FWHM) values are obtained by averaging measurements along four directions—horizontal, vertical, and two diagonals—on both the stacked image and the PSFs. We find that the stacked image exhibits FWHM consistently larger than those of the PSFs, confirming their extended nature. Importantly, the measured extended emission FWHMs are significantly broader than the PSF sizes. As mentioned in the previous subsection, the extended emission positions are not precisely at the pixel center, which could introduce a positional dispersion of at sub-pixel scale. However, this level of dispersion cannot account for the observed broadening of the stacked profiles we observed, indicating that the extended sizes are not due to PSF mismatches but rather reflect genuine extended emission.

To accurately measure this extended component, we fit a single Sérsic model to the stacked image. Likewise, the fitting on the individual source, we restrict the Sérsic index $(n) \in [1,4]$ to ensure physical plausibility, while allowing a wide range of the $R_{\rm eff}$. The PSFs used for reconstruction are selected from the B1 region in each band, and we find that the fitting results remain consistent using different PSFs across the field.

We list the fitting results in Table 1, the error bars of these numbers are given using the simulation tests (see Methods).The best-fit value for the fitted magnitudes of the extended components is 28.9, 29.2, 28.7, and 27.7 for F115W, F150W, F277W, and F444W, respectively, which is extremely faint and approaches the detection limit. Thus, it is difficult to recover through individual source fitting. Previous studies reported much smaller sizes of $\sim$30 pc for LRD[17], the size were strongly constrained by gravitational lensing and may be biased because the compact PS-dominated core was not removed during the fitting, whereas our stacked residuals isolate the extended component, yielding a PS-free size estimate.

Simulation tests. We conduct realistic simulation tests to verify the reliability of our fitting results. The simulation consists of two main steps: individual LRD image fitting and stacking of the data$-$PS residuals. In the image fitting step, we use the best-fit parameters derived from the 217 real analysis to generate the simulated images of Sérsic and the point source component using `lenstronomy`[57]. For each LRD target, we use the corresponding PSF both as the point source image and to convolve the model images, ensuring the observational conditions. To mimic realistic noise characteristics, we then inject Poisson noise into the simulated images and insert them into the empty sky region of the COSMOS-web field, thereby reproducing the true uncertainty level. These final images are then treated as realistic data during the fitting process. For each LRD, this simulation is repeated 10 times, and the results are averaged to produce a robust final simulated image.

Extended Data Figure 5 presents the results. The extended emission magnitude is well recovered, as shown in the top panel. However, due to the extreme faintness of the extended components in individual LRD, their structural parameters, particularly the R_{eff}, are poorly constrained. At the faint end, the extended emission magnitudes exhibit significant scatter in the residuals compared to the input values. More importantly, the measured R_{eff} shows almost no correlation with the true values, indicating that reliable size measurements for individual LRD are largely infeasible under current data conditions, further highlighting the limitations of relying solely on individual samples for extended source measurements.

To assess the robustness of our stacked results, we applied the same stacking procedure to simulated datasets. After subtracting the central point source, we stacked the residuals to create mock extended emission images, which were then fitted with a single Sérsic profile to recover extended emission properties. This process was repeated across 10 realizations, and the averaged results (shown as red dots in Extended Data Figure 5) are in excellent agreement with those derived from the real stacked image. Notably, the recovered R_{eff} is consistent with the real value (at 1-σ level and below 0.1 dex), indicating that, unlike individual fits, the stacking approach provides reliable and statistically meaningful constraints on the average extended emission properties of LRD.

An independent confirmation of extended emission with a second stacking method. In addition to the stacking method described in the main text (hereafter Method 1, or M1), we implemented an alternative approach to enhance the SNR and independently validate our results. We refer to this new approach as Method 2 (M2). The idea behind M2 is to first stack all LRD images, thereby enhancing the SNR of the extended component. Then, we perform image fitting on the stacked LRD image to assess whether the extended emission can be reliably detected. The detailed procedure is outlined below.

To ensure consistency between both methods, the selection criteria for the LRD sample used in M2 are identical to those applied in M1, comprising the final set of 217 LRDs. Prior to stacking, we applied interpolation to the individual images and shifted their positions to the pixel centers determined from the M1 fitting. This step is essential because the final stacked image is interpreted as a single point source, so precise alignment of the pre-stacked images is required. The image alignment was performed using the `shift()` function from the `SciPy` package. Due to the interpolation process, a slight distortion to the shape of the point source component is inevitable. After alignment, the images were stacked and averaged to produce the final combined LRD image.

We directly compare the sharpness of the stacked LRD images (M2) to that of the PSF and find that the PSF models have significantly smaller FWHM values than the combined LRD images at both short and long wavelengths. For example, the FWHMs of the LRD images are 3.38 and 5.84 compared to the PSF FWHMs of 1.93 and 5.32 for the F150W and F444W filters units in pixel, respectively. This significant broadening provides compelling evidence for the presence of an extended emission component beyond the point source.

Next, we perform image fitting on the stacked LRD. First, using the PS-only model, we detect a 'ring'-like residual feature similar to that observed in M1, further supporting the existence of extended emission (see Extended Data Figure 6). However, when fitting with the PS+Sérsic model, the Sérsic component tends to absorb nearly all the light. This behavior is likely caused by the interpolation and shifting process distorting the point source profile, which complicates accurate modeling of the point source component in the LRD. Therefore, M2 serves primarily as a qualitative confirmation of extended emission, rather than as a means for precise measurement of the LRD extended emission properties.

SED fitting analysis based on stellar model. Assuming the extended emission originates from a star, SED fitting is performed to estimate the stellar masses of our average host galaxies at $z \sim 6.45$ using the photometry and its uncertainty based on NIRCam imaging with four filters (F115W, F150W, F277W, and F444W) which straddle the rest-frame 4000 Å break.

We adopt a Kroupa IMF, which is consistent with the Chabrier IMF, in our analysis to allow direct comparison with the local black hole–host galaxy mass relations (e.g., ref. 35,36). Contributions of nebular emission lines from the host galaxies are also included with a uniform log ionization parameter $\log U$ over the range $[-3,-1]$. The star-formation history is modeled with an exponentially declining (τ-model) component. Four key parameters define the stellar population: age, τ, stellar metallicity, and dust attenuation A_V. We adopt a uniform prior on the stellar age in the range $[0.01, 0.85]$ Gyr, capped by the age of the Universe at $z = 6.45$. The e-folding timescale τ is allowed to vary between 0.01 and 0.85 Gyr, and the stellar mass formed is parameterized by $\log_{10}(M_*/M_\odot)$ ranging from 0.1 to 15. Stellar metallicity is allowed to vary between 0 and $2.5Z_\odot$. Dust attenuation is described by a Calzetti law, with A_V ranging from 0 to 5 mag. We adopt deliberately broad prior ranges to allow the SED fitting as much freedom as possible.

We use `bagpipes`[23] to perform the SED model fitting. This software generates a set of templates with a range of ages and metallicities according to the prior to fit a composite stellar population (CSP)-like star formation history. A random parameter sampling is performed through MCMC to infer the probability distribution of the SED parameters. For average host of LRD, the inferred values of $\log M_*$ are $8.91^{+0.10}_{-0.12} M_\odot$. In Figure 3, we present the best-fit SEDs of the average host of LRD, in which the MCMC inference indicates that the stellar mass is mildly sensitive to age and metallicity but is more sensitive to A_V. In addition, we apply the independent SED fitting code `gsf`[25] and obtain consistent results, with $\log M_* \sim 8.83^{+0.18}_{-0.23} M_\odot$, further confirming the robustness of our stellar mass estimates.

To investigate potential redshift evolution, we conducted an additional test by dividing the sample into two redshift bins: $5 < z < 6.4$ (1.19 - 0.87 Gyr) and $6.4 < z < 9$ (0.87 - 0.55 Gyr), containing 113 and 104 LRDs, respectively. Stacked SED were constructed for each bin, and the spectral fitting was performed using the `Bagpipes` code, assuming the same priors as in the main analysis. The median redshifts of the two subsamples are z = 5.92 and z = 7.04, respectively. The best-fit $\log(M_*/M_\odot)$ are $8.77^{+0.13}_{-0.15}$ and $9.16^{+0.10}_{-0.11}$, with corresponding sSFR of $\log(\mathrm{sSFR/yr^{-1}})$ = -8.71 and -8.57, suggesting comparable levels of star-forming activity per unit stellar mass.

SED fitting analysis based on nebular gas model. We further considered whether the extended emission in LRDs could arise from nebular gas[7]. We adopted the nebular emission templates provided by Chen et al.[7] and performed SED fitting via minimization. Our best-fit model, with a metallicity of approximately 0.1 $Z_\odot$ can broadly match the observed four-band photometry (see Figure 7). However, while Chen et al.(2025)[7] reported a detection of a strong [O III] emission line in one case, the fit here is still largely driven by other strong emission lines whose signatures have not been spectroscopically detected. Even when assuming a mixed contribution from gas-rich components and stellar populations, dedicated observations, particularly narrow- or medium-band imaging, are required to confirm the presence of these emission lines.

While the nebular gas model reproduces the overall SED shape, it cannot account for the extended F444W emission, a key observational constraint of this work. Moreover, the predicted strong narrow-line features are not evident in current data or previous studies, and the reduced χ^2 value ($\chi^2 \sim$2.089) for the nebular line fit is much higher than for the stellar population model ($\chi^2 \sim$1.508). Taken together, these factors suggest the stellar light scenario provides a more plausible explanation for the observed extended emission in LRDs.

Light variability. We identified 18 LRDs in our sample with multi-epoch imaging data, where the time separations between observations exceed 30 days. The shortest interval is approximately 58 days, while the longest extends to about one year. We performed preliminary photometric measurements to assess the magnitude differences between epochs.

In the F444W band, the maximum observed magnitude variation is less than 0.1 mag, with an average difference of only 0.015 mag. This is consistent with previous studies reporting no significant variability in LRDs[12,62]. After visually inspecting the images and excluding sources with large discrepancies caused by fitting artifacts, we find that the magnitude variations in other bands also remain below 0.2 mag. In the F115W band, we measure an average magnitude difference of 0.133 ± 0.127 mag, which is in good agreement with the variability amplitude of 0.12 ± 0.24 mag reported by ref. 13 in the rest-frame UV.

Data Availability

The JWST data are available from the COSMOS-Web survey. The catalog of LRDs can be accessed via DOI: `https://doi.org/10.48550/arXiv.2406.10341` or at `https://github.com/hollisakins/akins24_cw`.

Code Availability

The following software packages used in this work are publicly available:

- `galight`: `https://github.com/dartoon/galight`
- `bagpipes`: `https://github.com/JohannesBuchner/MultiNest`
- `gsf`: `https://github.com/mtakahiro/gsf.git`

Acknowlegements

X.D. and K.L acknowledge the National Key R&D Program of China (No. 2024YFC2207400). M.F. acknowledges funding from the European Union's Horizon 2020 research and innovation program under the Marie Sklodowska-Curie grant agreement No 101148925. L.C.H. was supported by the National Science Foundation of China (Grant No. 12233001) and the China Manned Space Program (CMS-CSST-2025-A09). K.I. acknowledges support from the National Natural Science Foundation of China (Grant No. 12233001), the National Key R&D Program of China (2022YFF0503401), and the China Manned Space Program (CMS-CSST-2025-A09). K.L acknowledges the National Natural Science Foundation of China (NSFC) No. 12222302. M.O. is supported by the Japan Society for the Promotion of Science (JSPS) KAKENHI Grant Number 24K22894. T.T. is supported by the Japan Society for the Promotion of Science (JSPS) KAKENHI Grant Number JP25KJ0750. B.Y. is supported by Xiaomi Foundation / Xiaomi Young Talents Program.

Author Contributions Statement

Y.Z. led the analysis of the LRD decomposition, residual stacking, and simulation tests, and contributed significantly to the preparation of the manuscript. X.D. conceived the idea of this study, led the SED fitting, and was also actively involved in writing the manuscript. L.Y. was responsible for the analysis of morphology-related properties and played a significant role in revising the manuscript. L.C.H. provided the nebular gas scenario and improved the stacking method. H.Y. suggested an alternative stacking approach (M2). C.C. contributed the gas model used in the fitting. All co-authors contributed to the discussion of the presented results and the preparation of the manuscript.

Competing Interests Statement

The authors declare no competing interests.

Extended Data

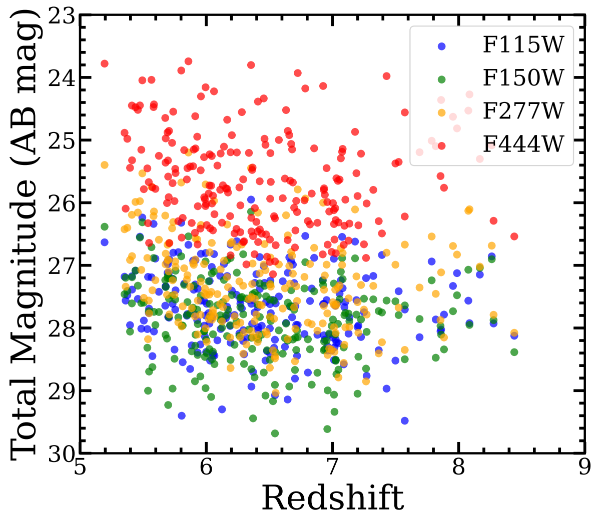

Extended Data Figure 1. Distribution of magnitude and redshift for the selected LRD sample in four bands. The sample includes 217 sources satisfying the criteria F115W - F150W < 0.8, total magnitude < 30, and $\chi^2 < 2$. Red, yellow, green, and blue dots represent F444W, F277W, F150W, and F115W, respectively. The sample spans a redshift range of $z = 5$–9, with source brightness in the short-wavelength bands approaching the detection limit.

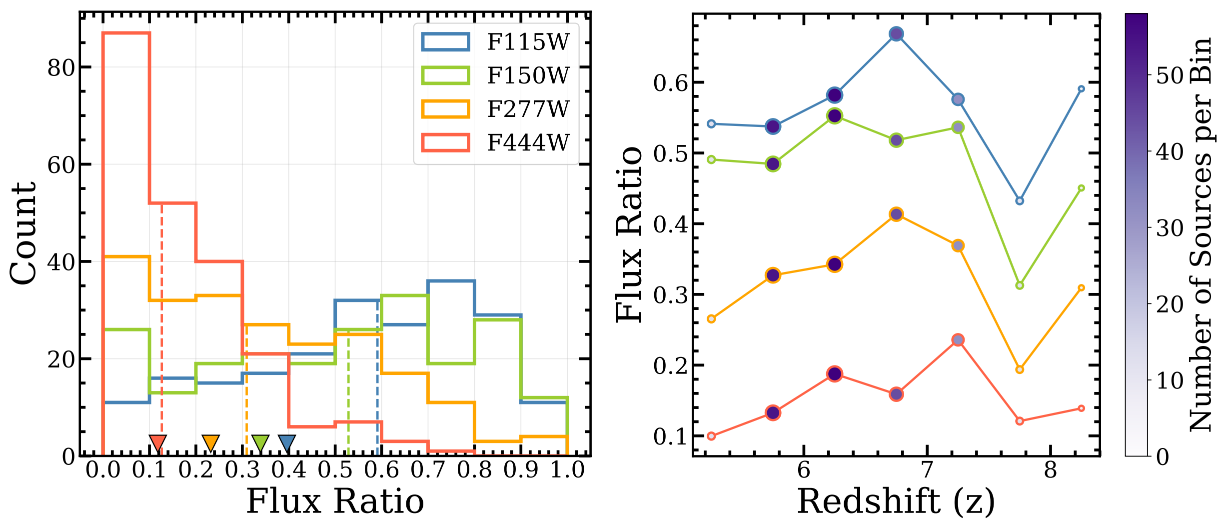

Extended Data Figure 2. Distribution of individual LRD extended emission to total flux ratio and the redshift evolution. *Left:* Histogram of the LRD extended emission to total flux ratio. The step histograms represent the distribution of ratio within 10% intervals. The dashed lines mark the median values of individual LRD, while the triangle symbols indicate the extended emission to total flux ratio of the corresponding averaged image in each band using the stacking method. *Right:* The position of each scatter point represents the mean extended emission to total flux ratio in a given redshift bin, while the color of the solid lines distinguishes different filters. The scatter points are color-coded according to the number of sources in each bin, as shown by the colorbar, and their marker size is proportional to the number of sources, such that larger markers indicate bins with more sources.

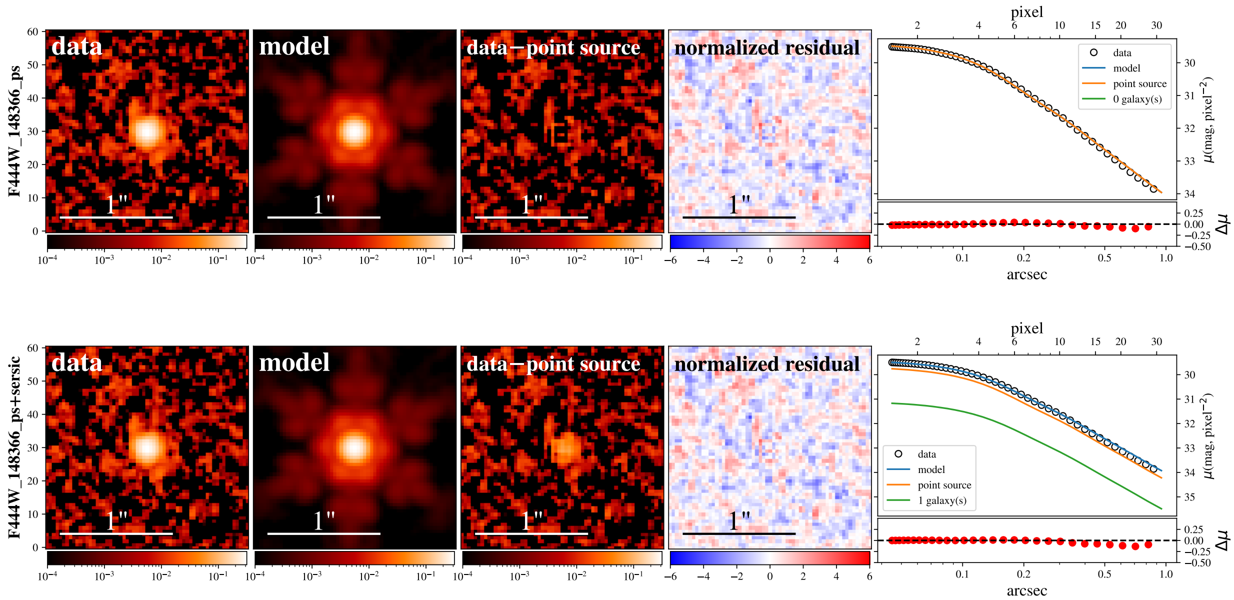

Extended Data Figure 3. Example of PS-only and PS+Sérsic fitting on an individual LRD. *Top:* Results from PS-only fitting. Panels from left to right: observed image (data), best-fit point source model (PS), residual image after subtracting the PS component (data−PS), normalized residual image, and the corresponding 1D surface brightness profile. *Bottom:* Results from PS+Sérsic fitting. Panels from left to right: observed image (data), best-fit composite model (PS+Sérsic), residual image after subtracting the PS component (data−PS), normalized residual image, and the corresponding 1D surface brightness profile.

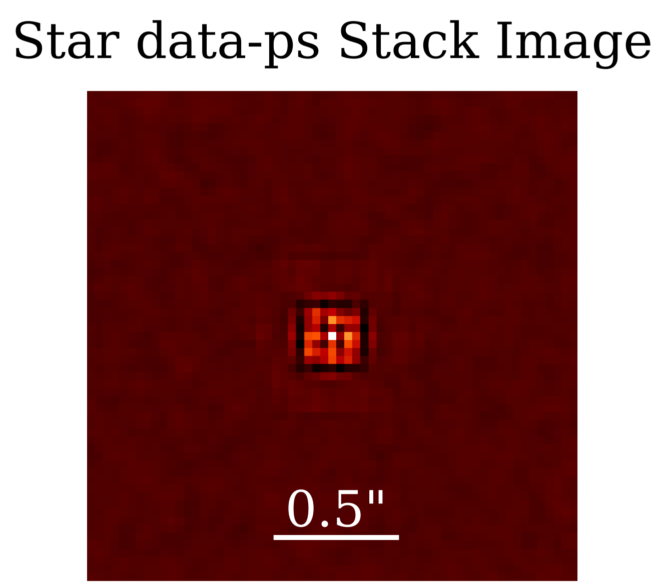

Extended Data Figure 4. Stacked residual image of 263 stars in the COSMOS-Web field after PS-only fitting. Each star was modeled using the corresponding PSF and stacked following the same procedure applied to the LRD sample. The residual shows no significant extended emission or ring-like features.

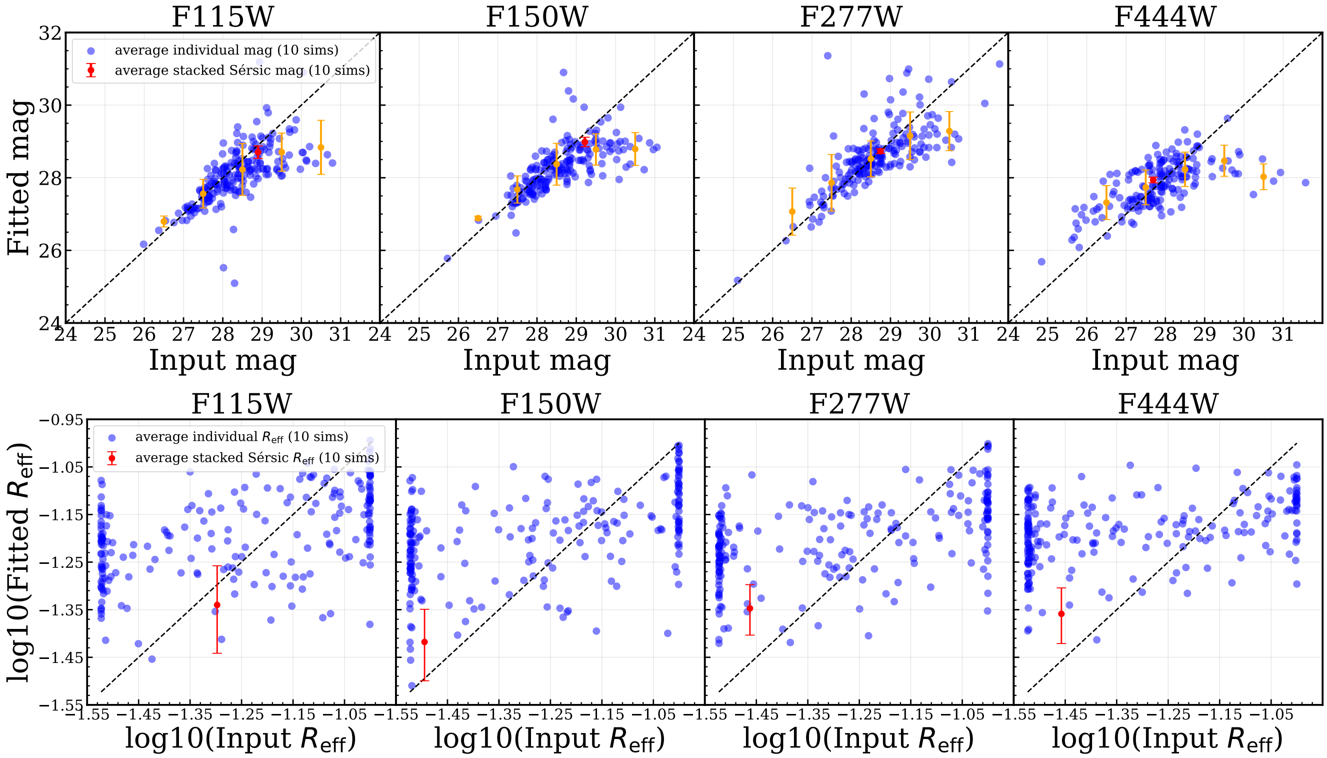

Extended Data Figure 5. Simulation results. *Top:* Comparison between the real total magnitude and the magnitude of the residual component obtained from simulations, shown for each band. *Bottom:* Comparison between $\log_{10}$ of the real $R_{\rm eff}$ and that derived from simulations. In both panels, the y-axis represents values derived from the real data, while the x-axis represents the mean result from 10 independent simulations per sample. Each blue dot corresponds to the average simulation output for one LRD sample. The red dot represents the inferred result from the final stacked image of 217 LRDs, averaged over 10 realizations, with error bars indicating the standard deviation. Note that red and blue points are derived from independent sets of simulations and do not share the same input realizations.

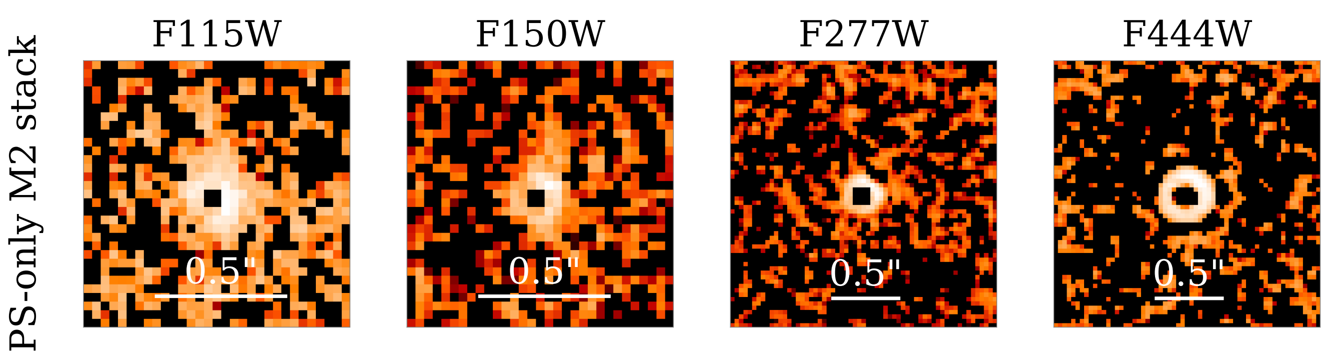

Extended Data Figure 6. Residual image after performing PS-only fitting on the Method-2 stacked image. Similar to the residuals obtained by stacking individual data−PS images, this approach reveals significant leftover emission after PS-only fitting. The central region exhibits signs of over-subtraction, indicating that a single point source model is insufficient to account for the full light distribution.

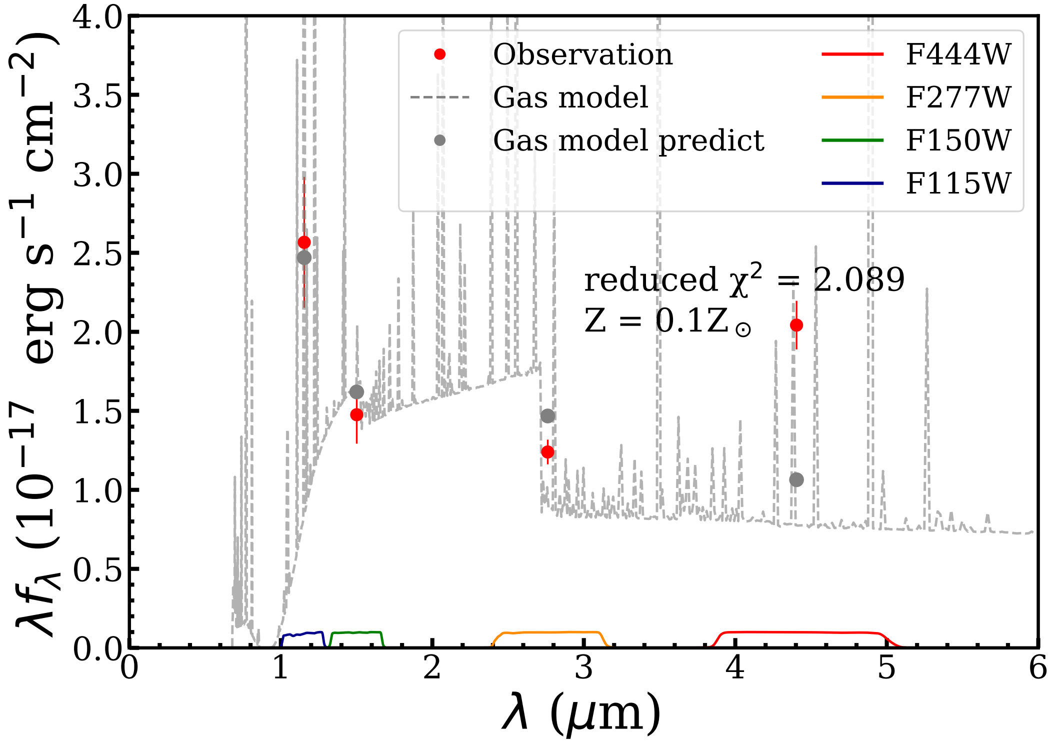

Extended Data Figure 7. SED fitting of the extended component with a nebular gas model. Red points with error bars represent stacked fluxes. The gray line shows the model spectrum, and the gray circle marks its best-fit prediction.

References

1. Furtak, L.J. and 31 colleagues 2023. JWST UNCOVER: Extremely Red and Compact Object at z_{phot} = 7.6 Triply Imaged by A2744. The Astrophysical Journal 952. doi:10.3847/1538-4357/acdc9d

2. Matthee, J. and 27 colleagues 2024. Little Red Dots: An Abundant Population of Faint Active Galactic Nuclei at $z \sim 5$ Revealed by the EIGER and FRESCO JWST Surveys. The Astrophysical Journal 963. doi:10.3847/1538-4357/ad2345

3. Greene, J. E. and 35 colleagues 2024. UNCOVER Spectroscopy Confirms the Surprising Ubiquity of Active Galactic Nuclei in Red Sources at $z > 5$. The Astrophysical Journal 964. doi:10.3847/1538-4357/ad1e5f

4. Rinaldi, P. and 25 colleagues 2025. Beyond the Dot: an LRD-like nucleus at the Heart of an IR-Bright Galaxy and its implications for high-redshift LRDs. arXiv e-prints. doi:10.48550/arXiv.2507.17738

5. Lin, X. and 11 colleagues 2025. Unravel the Puzzles of Little Red Dots: HST View on Local Analogs. HST Proposal, 18038.

6. Chen, C.-H., Ho, L. C., Li, R., Zhuang, M.-Y. 2024. The Host Galaxy (If Any) of the Little Red Dots. arXiv e-prints. doi:10.48550/arXiv.2411.04446

7. Chen, C.-H., Ho, L. C., Li, R., Inayoshi, K. 2025. The Physical Nature of the Off-centered Extended Emission Associated with the Little Red Dots. arXiv e-prints. doi:10.48550/arXiv.2505.03183

8. Tanaka, T. S. and 62 colleagues 2025. Discovery of a Little Red Dot candidate at $zrsim$10 in COSMOS-Web based on MIRI-NIRCam selection. arXiv e-prints. doi:10.48550/arXiv.2508.00057

9. Akins, H. B. and 40 colleagues 2024. COSMOS-Web: The over-abundance and physical nature of “little red dots”–Implications for early galaxy and SMBH assembly. arXiv e-prints. doi:10.48550/arXiv.2406.10341

10. Casey, C. M. and 85 colleagues 2023. COSMOS-Web: An Overview of the JWST Cosmic Origins Survey. The Astrophysical Journal 954. doi:10.3847/1538-4357/acc2bc

11. Labbe, I. and 31 colleagues 2025. UNCOVER: Candidate Red Active Galactic Nuclei at $3 < z < 7$ with JWST and ALMA. The Astrophysical Journal 978. doi:10.3847/1538-4357/ad3551

12. Kokubo, M., Harikane, Y. 2024. Challenging the AGN scenario for JWST/NIRSpec broad Hα emitters/Little Red Dots in light of non-detection of NIRCam photometric variability and X-ray. arXiv e-prints. doi:10.48550/arXiv.2407.04777

13. Tee, W. L., Fan, X., Wang, F., Yang, J. 2025. Lack of Rest-frame Ultraviolet Variability in Little Red Dots Based on HST and JWST Observations. The Astrophysical Journal 983. doi:10.3847/2041-8213/adc5e3

14. Franco, M. and 39 colleagues 2025. COSMOS-Web: Comprehensive Data Reduction for Wide-Area JWST NIRCam Imaging. arXiv e-prints. doi:10.48550/arXiv.2506.03256

15. Bertin, E. 2011. Automated Morphometry with SExtractor and PSFEx. Astronomical Data Analysis Software and Systems XX 442, 435.

16. Ding, X. et al. The Mass Relations between Supermassive Black Holes and Their Host Galaxies at $1 < z < 2$ HST-WFC3. *Astrophys. J.* **888**, 37 (2020)

17. Furtak, L. J. and 37 colleagues 2024. A high black-hole-to-host mass ratio in a lensed AGN in the early Universe. Nature 628, 57–61. doi:10.1038/s41586-024-07184-8

18. Killi, M. and 12 colleagues 2024. Deciphering the JWST spectrum of a 'little red dot' at z $\sim$ 4.53: An obscured AGN and its star-forming host. Astronomy and Astrophysics 691. doi:10.1051/0004-6361/202348857

19. Sérsic, J. L. Boletin de la Asociacion Argentina de Astronomia La Plata Argentina, **6**, 41-43 (1963)

20. Brooks, M. and 15 colleagues 2024. Here There Be (Dusty) Monsters: High Redshift AGN are Dustier Than Their Hosts. arXiv e-prints. doi:10.48550/arXiv.2410.07340

21. Tanaka, T. S. and 46 colleagues 2024. Discovery of dual "little red dots" indicates excess clustering on kilo-parsec scales. arXiv e-prints. doi:10.48550/arXiv.2412.14246

22. Naidu, R. P. and 50 colleagues 2025. A "Black Hole Star" Reveals the Remarkable Gas-Enshrouded Hearts of the Little Red Dots. arXiv e-prints. doi:10.48550/arXiv.2503.16596

23. Carnall, A. C., McLure, R. J., Dunlop, J. S., Davé, R. 2018. Inferring the star formation histories of massive quiescent galaxies with BAGPIPES: evidence for multiple quenching mechanisms. Monthly Notices of the Royal Astronomical Society 480, 4379–4401. doi:10.1093/mnras/sty2169

24. Wang, B. and 24 col2025NatAs...9..271Sleagues 2024. RUBIES: JWST/NIRSpec Confirmation of an Infrared-luminous, Broad-line Little Red Dot with an Ionized Outflow. arXiv e-prints. doi:10.48550/arXiv.2403.02304

25. Morishita, T., et al. Massive Dead Galaxies at z $\sim$ 2 with HST Grism Spectroscopy. I. Star Formation Histories and Metallicity Enrichment. *Astrophys. J.* **877**, 141 (2019)

26. Morishita, T. and 7 colleagues 2025. A Nitrogen-rich AGN Powering a Large Ionizing Bubble at z=8.63. arXiv e-prints. doi:10.48550/arXiv.2508.01372

27. Xiao, M. and 32 colleagues 2025. No [CII] or dust detection in two Little Red Dots at $z_{spec} > 7$. arXiv e-prints. doi:10.48550/arXiv.2503.01945

28. Setton, D. J. and 35 colleagues 2025. A confirmed deficit of hot and cold dust emission in the most luminous Little Red Dots. arXiv e-prints. doi:10.48550/arXiv.2503.02059

29. Akins, H. B. and 9 colleagues 2025. Tentative detection of neutral gas in a Little Red Dot at $z = 4.46$. arXiv e-prints. doi:10.48550/arXiv.2503.00998

30. Donevski, D. and 13 colleagues 2020. In pursuit of giants. I. The evolution of the dust-to-stellar mass ratio in distant dusty galaxies. Astronomy and Astrophysics 644. doi:10.1051/0004-6361/202038405

31. Casey, C. M. and 11 colleagues 2025. An upper limit of 10^6 $M_\odot$ in dust from ALMA observations in 60 Little Red Dots. arXiv e-prints. doi:10.48550/arXiv.2505.18873

32. Yang, L., Kartaltepe, J. S., Franco, M., et al. 2025, , COSMOS-Web: Unraveling the Evolution of Galaxy Size and Related Properties at $2 < z < 10$, arXiv:2504.07185. doi:10.48550/arXiv.2504.07185

33. Harikane, Y. and 8 colleagues 2023. A JWST/NIRSpec First Census of Broad-line AGNs at z = 4-7: Detection of 10 Faint AGNs with M $_{BH}$ 10^6-10^8 M $_\odot$ and Their Host Galaxy Properties. The Astrophysical Journal 959. doi:10.3847/1538-4357/ad029e

34. Kocevski, D. D. and 56 colleagues 2024. The Rise of Faint, Red AGN at $z > 4$: A Sample of Little Red Dots in the JWST Extragalactic Legacy Fields. arXiv e-prints. doi:10.48550/arXiv.2404.03576

35. Kormendy, J., Ho, L. C. 2013. Coevolution (Or Not) of Supermassive Black Holes and Host Galaxies: Supplemental Material. arXiv e-prints. doi:10.48550/arXiv.1308.6483

36. Greene, J. E., Strader, J., Ho, L. C. 2020. Intermediate-Mass Black Holes. Annual Review of Astronomy and Astrophysics 58, 257–312. doi:10.1146/annurev-astro-032620-021835

37. Suh, H. and 15 colleagues 2025. A super-Eddington-accreting black hole ~1.5 Gyr after the Big Bang observed with JWST. Nature Astronomy 9, 271–279. doi:10.1038/s41550-024-02402-9

38. Prole, L. R., Regan, J. A., Whalen, D. J., Glover, S. C. O., Klessen, R. S. 2024. Halo mergers enhance the growth of massive black hole seeds. Astronomy and Astrophysics 692. doi:10.1051/0004-6361/202452486

39. Inayoshi, K., Visbal, E., Haiman, Z. 2020. The Assembly of the First Massive Black Holes. Annual Review of Astronomy and Astrophysics 58, 27–97. doi:10.1146/annurev-astro-120419-014455

40. Inayoshi, K. 2025. Little Red Dots as the Very First Activity of Black Hole Growth. The Astrophysical Journal 988. doi:10.3847/2041-8213/adea66

41. Rusakov, V. and 16 colleagues 2025. JWST's little red dots: an emerging population of young, low-mass AGN cocooned in dense ionized gas. arXiv e-prints. doi:10.48550/arXiv.2503.16595

42. Greene, J. E. and 29 colleagues 2025. What you see is what you get: empirically measured bolometric luminosities of Little Red Dots. arXiv e-prints. doi:10.48550/arXiv.2509.05434

43. Übler, H. and 22 colleagues 2023. GA-NIFS: A massive black hole in a low-metallicity AGN at $z \sim 5.55$ revealed by JWST/NIRSpec IFS. Astronomy and Astrophysics 677. doi:10.1051/0004-6361/202346137

44. Goulding, A. D. and 29 colleagues 2023. UNCOVER: The Growth of the First Massive Black Holes from JWST/NIRSpec-Spectroscopic Redshift Confirmation of an X-Ray Luminous AGN at z = 10.1. The Astrophysical Journal 955. doi:10.3847/2041-8213/acf7c5

45. Kokorev, V. and 31 colleagues 2023. UNCOVER: A NIRSpec Identification of a Broad-line AGN at z = 8.50. The Astrophysical Journal 957. doi:10.3847/2041-8213/ad037a

46. Stone, M. A., Lyu, J., Rieke, G. H., Alberts, S., Hainline, K. N. 2024. Undermassive Host Galaxies of Five $z \sim 6$ Luminous Quasars Detected with JWST. The Astrophysical Journal 964. doi:10.3847/1538-4357/ad2a57

47. Yue, M. and 8 colleagues 2024. EIGER. V. Characterizing the Host Galaxies of Luminous Quasars at $z \gtrsim 6$. The Astrophysical Journal 966. doi:10.3847/1538-4357/ad3914

48. Ding, X. and 43 colleagues 2023. Detection of stellar light from quasar host galaxies at redshifts above 6. Nature 621, 51–55. doi:10.1038/s41586-023-06345-5

49. Li, R., Ho, L. C., Chen, C.-H. 2025. The Dichotomy in the Nuclear and Host Galaxy Properties of High-redshift Quasars. arXiv e-prints. doi:10.48550/arXiv.2505.12867

50. Casey, C. M. and 41 colleagues 2024. COSMOS-Web: Intrinsically Luminous $z \gtrsim 10$ Galaxy Candidates Test Early Stellar Mass Assembly. The Astrophysical Journal 965. doi:10.3847/1538-4357/ad2075

51. Scoville, N. and 21 colleagues 2007. The Cosmic Evolution Survey (COSMOS): Overview. The Astrophysical Journal Supplement Series 172, 1–8. doi:10.1086/516585

52. Rieke, M. J. and 54 colleagues 2023. Performance of NIRCam on JWST in Flight. Publications of the Astronomical Society of the Pacific 135. doi:10.1088/1538-3873/acac53

53. Bushouse, H. and 28 colleagues 2023. JWST Calibration Pipeline. Zenodo. doi:10.5281/zenodo.10022973

54. Rest, A. and 7 colleagues 2023. arminrest/jhat: The JWST HST Alignment Tool (JHAT). Zenodo. doi:10.5281/zenodo.7892935

55. Bagley, M. B. and 39 colleagues 2023. CEERS Epoch 1 NIRCam Imaging: Reduction Methods and Simulations Enabling Early JWST Science Results. The Astrophysical Journal 946. doi:10.3847/2041-8213/acbb08

56. Koekemoer, A. M. and 13 colleagues 2007. The COSMOS Survey: Hubble Space Telescope Advanced Camera for Surveys Observations and Data Processing. The Astrophysical Journal Supplement Series 172, 196–202. doi:10.1086/520086

57. Birrer, S., et al. lenstronomy II: A gravitational lensing software ecosystem. *The Journal of Open Source Software* **6**, 3283 (2021)

58. Bradley, L., Sipőcz, B., Robitaille, T., et al. astropy/photutils: 1.4.0 Zenodo 6385735B (2022)

59. Ding, X., Birrer, S., Treu, T., Silverman, J. D. 2021. Galaxy shapes of Light (GaLight): a 2D modeling of galaxy images. arXiv e-prints. doi:10.48550/arXiv.2111.08721

60. Tanaka, T. S. and 27 colleagues 2025. The M_{BH}–M_* Relation up to $z \sim 2$ through Decomposition of COSMOS-Web NIRCam Images. The Astrophysical Journal 979. doi:10.3847/1538-4357/ad9d0a

61. Zhuang, M.-Y., Li, J., Shen, Y. 2024. Active Galactic Nuclei and Host Galaxies in COSMOS-Web. I. NIRCam Images, Point-spread-function Models and Initial Results on X-Ray-selected Broad-line AGNs at $0.35 \lesssim z \lesssim 3.5$. The Astrophysical Journal 962. doi:10.3847/1538-4357/ad1517

62. Zhang, Z., Jiang, L., Liu, W., Ho, L. C. 2025. Analysis of Multi-epoch JWST Images of $\sim$300 Little Red Dots: Tentative Detection of Variability in a Minority of Sources. The Astrophysical Journal 985. doi:10.3847/1538-4357/adcb3e